Structural changes in the lithium cobalt dioxide electrode: A combined approach with cluster expansion and Bayesian optimization

Fumiaki Kuroda,* Satoshi Hagiwara, and Minoru Otani
Center for Computational Sciences, University of Tsukuba, 1-1-1, Tenno-dai, Tsukuba, Ibaraki 305-8577, Japan

(Received 6 April 2023; accepted 9 October 2023; published 13 November 2023)

Lilithium cobalt dioxide ($LiCoO_2$) is a promising cathode material for rechargeable lithium-ion batteries (LIBs). To improve the electrochemical performance of LIBs, we theoretically investigated the structural changes in a $LiCoO_2$ electrode through the thermodynamic convex hull analysis. To construct the convex hull, we combined cluster expansion and Bayesian optimization (BO) with high-throughput density functional theory (DFT) calculations. To improve the BO efficiency, we used hull distance as the target variable of BO, which considerably reduced the number of DFT calculations. At 300 K, the O_2 gas release by the convex hull was confirmed. The defective stoichiometry of CoO_{2-y} deteriorated the layered structure of CoO_2 and prevented the Li^+ ion migration. Therefore, we considered that the formation of CoO_{2-y} contributed to the cathode degradation. Our findings will provide useful insights into the prevention of LIB degradation.

DOI: 10.1103/PhysRevMaterials.7.115402

I. INTRODUCTION

To address global warming problems and reduce the use of fossil fuels, it is important to develop technologies that convert energy from renewable and sustainable sources to electrical power is one of the significant issues. Rechargeable lithium-ion batteries (LIBs) are among the most efficient energy storage devices [1–3]. In 1981, Mizushima *et al*. proposed lithium cobalt oxide (LCO, $LiCoO_2$) as a cathode material for LIB [4], and it has been widely used as a typical LIB electrode in recent years. However, LIB with the LCO electrode utilizes only half of the theoretical capacity of LCO owing to its thermal instability in high-voltage operations [5–10]. In a high-voltage operation, LCO releases O_2 gases, and the resulting oxygen-deficient LCO (Li_xCoO_{2-y}) degrades the electrochemical performance of LIB [6,8–11]. In the degraded LIBs, the spinel structure of Co_3O_4 is frequently observed by x-ray spectroscopy and scanning transmission electron microscopy [8,9]. Therefore, to improve the available specific capacity and lifetime of LIBs, it is beneficial to elucidate the relationship between the structural changes in LCO during charge/discharge cycling and battery degradation.

To elucidate the structural changes in materials, an analysis of the thermodynamic convex hull is a useful method, which is defined by the formation energies of the most stable structures at each composition ratio. Density functional theory (DFT) [12,13] is a powerful tool for theoretically predicting the convex hull for the desired combination of the material elements [14–16]. However, for the direct construction of the convex hull, we need to exhaustively evaluate the formation energies of the target material at each composition ratio, which incurs a huge computational cost owing to the semi-infinite number of potential material elements. The cluster expansion (CE) method is one of the efficient approaches to consider the composition-ratio dependence of the formation energy [17–26]. However, because the O-deficient structure undergoes a large structural displacement, the simple use of the conventional CE fails to predict the formation energies for such system [27,28].

Recently, to construct a convex hull for general materials, Seko *et al*. combined the CE method with Bayesian optimization (CE+BO) [29], and the CE+BO method with DFT calculations succeeded in predicting the stability of the O-deficient perovskite structures with large structural displacements. Although assuming parent structures is necessary, the CE+BO method enables us to alter the number of atoms and the composition ratio for the target compounds. Thus, the CE+BO method can efficiently search for thermodynamically stable phases of materials by constructing a convex hull concerning the formation energies of the compounds. On the other hand, there are several methods to find globally stable structures without assuming parent structures, e.g., evolutionary algorithm and particle-swarm optimization-based methods, and so on [30–32]. These methods enable us to obtain the thermodynamically stable structure at the given composition ratio. However, they require huge computational costs to construct the convex hull in the entire composition space. Therefore, we need to use these structure prediction methods depending on the situation.

In this study, to elucidate the structural changes of the LCO electrode, we constructed a convex hull of the entire Li-Co-O phase using the CE+BO method and proposed a simple method to accelerate the convergence of CE+BO. This paper is organized as follows: In section II, we discuss the proposed CE+BO framework, analysis method for convex-hull, and computational details. Section III shows the results of a benchmark for efficiency of CE+BO, the voltage profile of the LCO obtained by the convex-hull analysis with and without

*kuroda@ccs.tsukuba.ac.jp

a finite temperature effect. In Sec. IV, we discuss the origin of the efficient convex hull construction using the CE+BO method and the relationship between the weight density of metastable CoO_{2-y} and the battery degradation. Finally, we provide summary of our study in Sec. V.

II. METHOD

A. CE+BO method

Here, we briefly discuss the CE+BO method and our proposed method to accelerate the convergence of CE+BO. The CE theory is formally exact to model the DFT total energies as a function of composition ratio with crystal structure information, by using a linear regression of a series of cluster correlation. Practically, the fourth-order of the cluster series has been used, which can well reproduce the formation energies and predict the stable structures of rigid lattice systems such as Li_xCoO_2 [33–35]. However, for Li_xCoO_{2-y} system, we can not simply apply the conventional CE method due to the limit of finite cluster series. The CE+BO method using a nonlinear regression compensates the incompleteness of a linear regression of the CE model with in the finite cluster series [36], which helps to select candidates for constructing the convex hull from numerous structures [29]. Therefore, we can predict the the convex hull by iteratively obtaining stable structures of Li_xCoO_{2-y} using CE+BO. The original CE+BO (BO1) used the correlation functions as the descriptors of BO and formation energy (E_f) as the target variable of the BO to represent the convex hull. To accelerate the iterative construction of the convex hull by CE+BO, we set the hull distance (E_{hd}) as the target variable (BO2), where the definition of E_{hd} is the formation energy measured from the envelope of the convex hull. In BO2, we note that the previously learned target values are also updated when the new stable structures are found in the current BO iteration because the reference energy of E_{hd} is updated. Further details are summarized in the Supplemental Material (SM) [37], and Refs. [38–43] are cited in the SM.

B. Voltage profile

We explain the thermodynamic method used to compute the voltage profile of the LCO electrode measured using the Li electrode. The electrochemical reactions for the formation of Li_xCoO_{2-y} is $Li_{x'}CoO_{2-y'} + (x-x')Li^+ + (y'-y)/2O_2 + (x-x')e^- \rightarrow Li_xCoO_{2-y}$. When we use the Li electrode as a reference, whose electrochemical reaction is $Li \rightarrow Li^+ + e^-$, the charge/discharge reactions can be be simplified as follows:

$$Li_{x'}CoO_{2-y'} + (x-x')Li + \frac{y'-y}{2}O_2 \rightarrow Li_xCoO_{2-y}. \quad (1)$$

The electromotive force V between LCO and Li metal for the reaction (1) is determined by

$$V = -\frac{G_{Li_xCoO_{2-y}} - G_{Li_{x'}CoO_{2-y'}} - (x-x')G_{Li} - (y'-y)G_{O_2}/2}{(x-x')F}, \quad (2)$$

where F is the Faraday constant. $G_{Li_xCoO_{2-y}}$, G_{Li}, and G_{O_2} are the formation Gibbs free energies of Li_xCoO_{2-y}, Li metal, and O_2 molecule, respectively. When the battery operation is sufficiently slow against the reaction (1), the charge/discharge reaction follows the minimum free-energy path for the stable phases of the different concentrations of Li. Thus, we can compare the results of Eq. (2) using the convex hull to the measured voltage profile of Li_xCoO_2. Here, we approximated the Gibbs free energies of the components by the DFT total energies, i.e., pressure × volume and entropy × temperature terms were neglected in otherwise specified. This approximation well reproduces the experimental electromotive force [33–35].

C. Computational details

We summarize the computational details of DFT and CE+BO methods. All DFT calculations were carried out using the Quantum ESPRESSO package [44,45] within a framework of the plane-wave basis sets and ultrasoft pseudopotential [46,47]. The cutoff energies for the wave function and augmented charge were set to 70 and 700 Ry, respectively. The generalized gradient approximation using the Perdew-Burke-Ernzerhof scheme [48] was used for exchange-correlation potentials and the on-site Hubbard-U correction [49] with an effective U of 2 eV was applied to the Co $3d$ state. Long-range van der Waals interactions were considered through a semiempirical correction within the optB86 scheme [50]. For all structures, we performed lattice and geometry optimizations and subtracted 1.36 eV from the total energy of the O_2 molecule, which enabled the reproduction of the experimental formation energy [51].

In CE+BO, we performed the BO procedure with a Gaussian process (GP) model using the PYSBO program package [52–56], and the cluster correlation function was determined using the ICET program [22]. In BO with a machine learning, to evaluate the acquisition function with the expected improvement, we used a GP model using a Gaussian kernel function with a 1000 l-dimensional feature vector [52]. We prepared the initial structures from the parent structures using the Hart's supercell approach [57,58]. To generate the initial structures for CE+BO, we adopted three experimentally observed structures [4,59,60] as the parent structures, that is, O3 type, O1 type, and H13 type of layered Li_xCoO_2, respectively (Fig. 1). The O1 and O3 structures are ABAB and ABCABC stacked layers, respectively, and H13 is a mixture of O1 and O3 structures. In addition, the spinel-type of Co_3O_4 was also used as the reference state for phase stability. The supercell sizes of $N_s \leqslant 6$, $N_s \leqslant 6$, and $N_s \leqslant 3$ were used for the O1-, O3-, and H13-type structures, respectively. The difference in the upper limit of N_s was due to the difference in the number of atoms in each supercell. The ranges of x and y were assumed as follows: $(0 \leqslant x \leqslant 1,\ 0 \leqslant y \leqslant 1/3)$, $(0 \leqslant y \leqslant 1/2)$, and $(0 \leqslant x \leqslant 1/2,\ 0 \leqslant y \leqslant 1/4)$ for the O3, O1, and H13 types, respectively.

III. RESULTS

A. Benchmarking of CE+BO method

First, we investigated the convergence behaviors of the convex-hull construction for the CE+BO methods. As a reference for the convex hull of LCO, we carried out

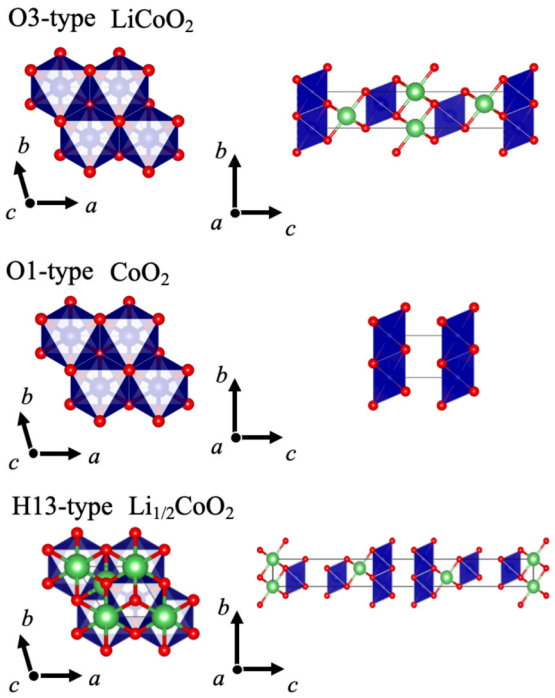

FIG. 1. Crystal structures of O3, O1 and H13 types of layered Li_xCoO_2. The green, blue and red balls represent Li, Co and O, respectively. The VESTA package was used to visualize the crystal structures throughout this study [61].

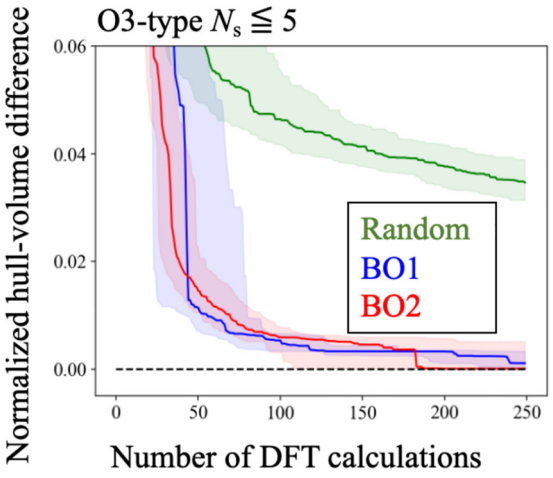

FIG. 2. Convergence behavior of convex hull as a function of the number of DFT calculations. The green, blue and red curves denote the median values of 100 BO simulations for random search, BO1, and BO2, respectively. The top and bottom of the shaded range are 25 and 75% of the interquartile range of 100 BO simulations, respectively.

comprehensive DFT calculations without CE+BO for all candidate structures generated with a supercell size of $N_s \leqslant 5$; the O3 parent structure were only used to reduce the benchmarking cost. Consequently, we confirmed the convergence of 2446 structures of the total 2693 structures and constructed the "true" convex hull using their formation energies. To consider the efficiency of CE+BO, we defined a normalized hull-volume difference (NHVD) as the difference in the convex-hull volumes between the predicted convex hull by CE+BO and the "true" convex hull. Therefore, when NHVD was zero, the CE+BO calculation reproduced the "true" convex hull. In this benchmarking study, we performed 100 independent BO simulations by selecting five different initial structures from the total structures to obtain the statistically converged result.

Figure 2 shows the convergence behavior of NHVD as a function of the number of performed DFT calculations. BO1 and BO2 can find stable structures faster than a random search. Although the NHVD of BO1 rapidly decreases compared with that of BO2, BO1 does not find the "true" convex hull until 250 DFT-calculation steps. In contrast, the NHVD of BO2 reaches zero in 200 DFT-calculation steps. Thus, we confirmed that BO2 sufficiently reduced the number of DFT calculations required to construct the convex hull.

B. Phase diagram and voltage profile for Li-Co-O system

Figures 3(a) and 3(c) show the result of the convex hull obtained from the O1-, O3-, and H13-type structures at a temperature of 0 K. We found that the O1-type of CoO_2 and the H13-type derivative $Li_{1/6}CoO_2$ are stable at low Li concentrations. These O1-type and H13-type derivative structures are consistent with the experimentally observed structures [59,60,62]. Furthermore, the calculated convex hull indicates that the formation of O_2-gas is not a thermodynamically favored pathway, that is, the formation energy of O1-type CoO_2 is lower than that of the CoO_{2-y} with O_2 gas. Thus, the O_2 gas is not released at the LCO electrode during the charge/discharge cycles at a temperature of 0 K. From the convex hull analysis, we determine the voltage profile using Eq. (2), as shown in Fig. 3(e). The calculated voltage profile is in reasonable agreement with the experimental result [62]; we found that the voltage steps at $x = 1/6$ and $1/2$ are also consistent with those of the experiment. In the stable $Li_{1/2}CoO_2$ structure, the Li atoms exhibit two-dimensional (2D) zigzag ordering, which is consistent with earlier theoretical study [34]. However, the experimentally observed structure of $Li_{1/2}CoO_2$ was the row-ordered Li [2]. According to the previous theoretical study, the energy difference between these two ordered structures is less than 1 meV/atom. This energy difference is because the number of the first nearest Li-Li bonds in the in-plane of the row-ordered structure is the same as that in the zigzag structure. Thus, to discuss the stability of $Li_{1/2}CoO_2$, we might consider the additional terms to the internal energy by DFT such as the lattice vibrations [63].

Figures 3(b) and 3(d) show the results for the convex hull at a temperature of 300 K, where the finite temperature effect is considered through the entropy term of the O_2 molecule. Because the entropy term contributes to a decrease in the chemical potential of the O_2 molecule, O-rich compounds such as CoO_2 and $Li_{1/6}CoO_2$ become unstable (these structures are stable at 0 K). As a result, a three-phase separation with the formation of O_2 gas, $Li_{1/3}CoO_2$, and $CoO_{5/3}$ is observed. Thus, the formation of O_2 gas from the LCO

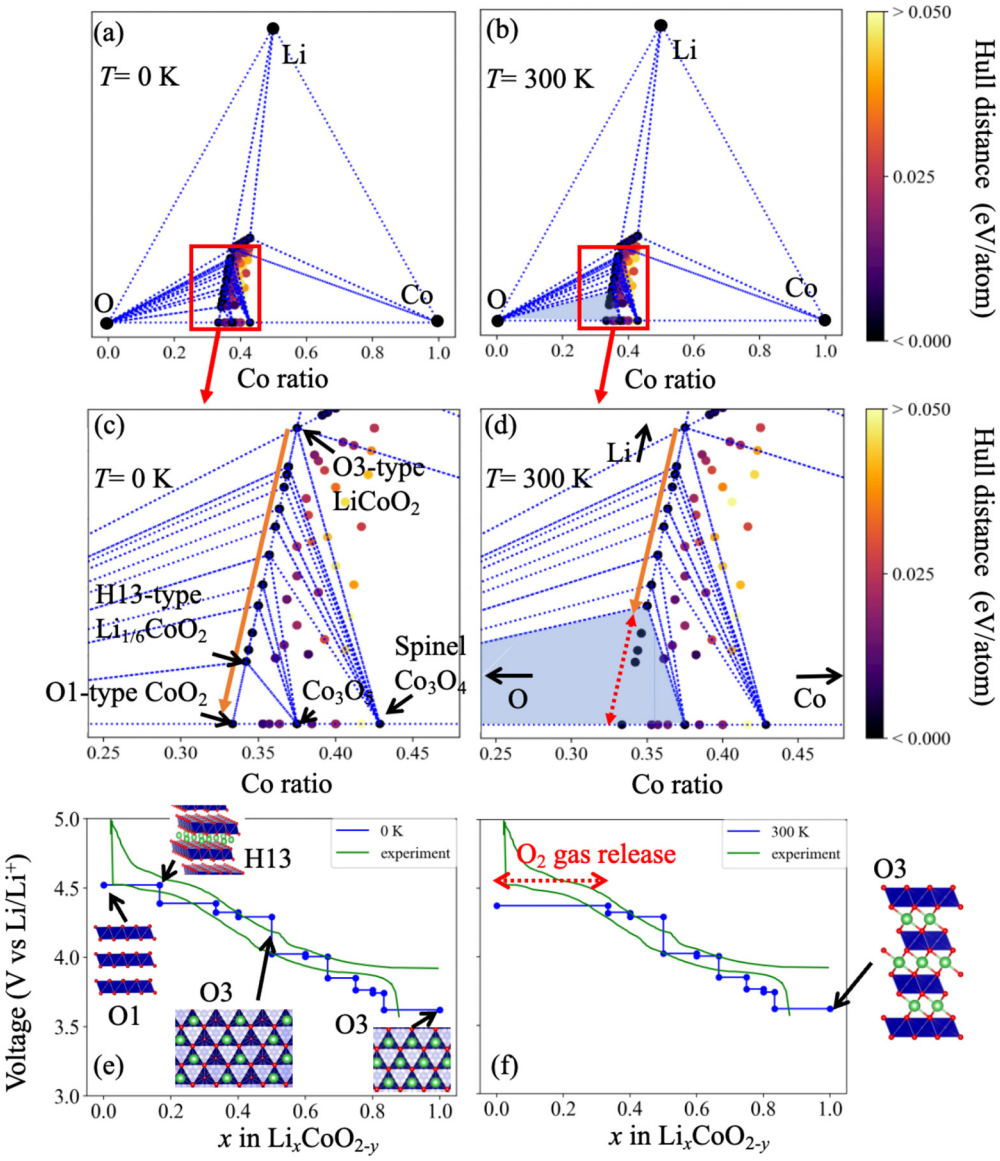

FIG. 3. Convex hulls in the Li-Co-O phase at (a, c) 0 K and (b, d) 300 K, and voltage profiles at (e) 0 K and (f) 300 K. The orange arrows denote the ideal charge reaction direction from $LiCoO_2$ to CoO_2 and the blue-shaded region represents the three-phase separation area. The experimental voltage profile is obtained from the paper [62].

electrode is due to a free energy shift at a finite temperature. Figure 3(f) shows the result of the voltage profile at 300 K. The calculated voltage below $x = 1/3$ is lower than that at 0 K, and the voltage step at $x = 1/6$ vanishes. These results were attributed to the structural change of LCO with the O_2 gas formation. Recently, Sun *et al*. observed the depth profile for the composition ratio of O to Co in an LCO electrode using electron-energy loss spectroscopy [9]. A decrease in the composition ratio of O, ranging from the outer-most surface to a depth of approximately 100 nm from the electrode surface, was observed, and its magnitude depended on the operation temperature. The decrease in O content in LCO at a low Li concentration could explain the aforementioned experimental findings. Therefore, we considered that the three-phase separation with the O_2 gas release contributed to the structural degradation of the LCO electrode.

C. Geometries of metastable CoO_{2-y}

According to the experimental and theoretical results [64–67], metastable structures can be formed and observed over experimental timescales. For LCO, during charge/discharge cycling, metastable structures may be formed and cause the battery degradation. Therefore, we investigate not only stable but also metastable structures of CoO_{2-y}. Figure 4 shows the results of weight densities for metastable structures of CoO_{2-y} as a function of the content of O-deficient stoichiometry. Here, stable $CoO_{5/3}$ ($y = 1/3$) consists of the convex hull, and we define the metastable structure as CoO_{2-y}, which satisfies the criterion of $E_{hd} \leqslant 0.070$ eV/atom, as discussed by Sun *et al*. [64]. Detailed information on the metastable structures of CoO_{2-y} and their E_{hd} are summarized in the SM [37]. For $y < 1/4$, the lack of O induces a large displacement and migration of both Co and

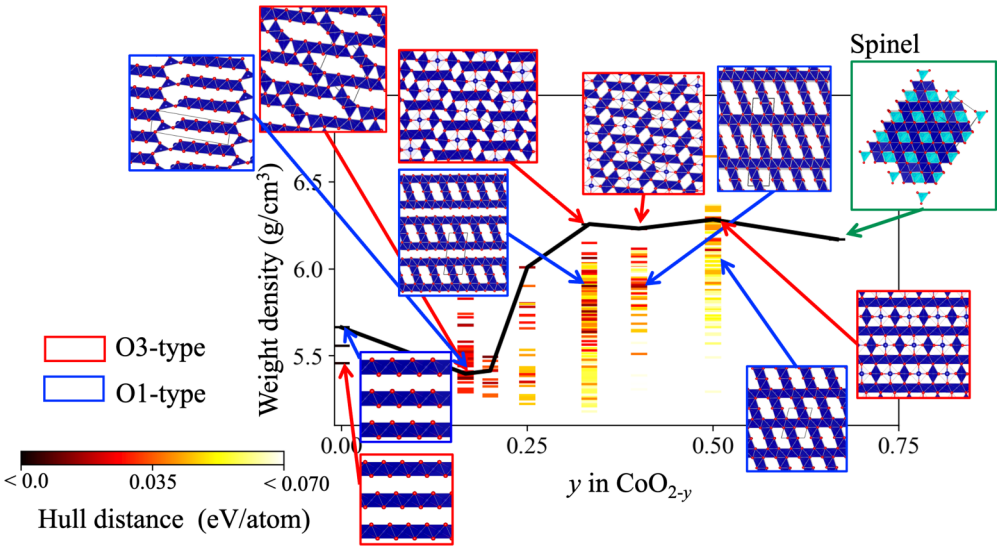

FIG. 4. Weight density of metastable CoO_{2-y} structures as a function of the content of O-deficient stoichiometry. The crystal structures with red, blue, and green frames represent the O3-type derivative, O1-type derivative, and spinel structures, respectively. The black line connects the weight densities of the most stable structures at each composition.

O atoms from the parent structures. Although the change in the weight density is relatively small, the 2D-layered structure of the parent CoO_2 starts to collapse, as shown in Fig. 4. Moreover, when more O_2 gas is released ($1/4 \leqslant y \leqslant 1/2$), the weight density of the most stable structures increases by 15%, which is close to that of the spinel Co_3O_4. In this region, the 2D-layered structure of CoO_2 completely disappears; thus, the increase in the weight density corresponds to the deterioration of the 2D-layered structure.

IV. DISCUSSION

A. Efficiency of CE+BO method

The difference in the convergence between BO1 and BO2 (Fig. 2) was attributed to the characterization of the convex hull within the BO framework, that is, the difference in the choice of target variables (Fig. 5). The E_f used in BO1 was the relative energy measured from the vertices of the Li-Co-O phase triangle; the E_f value was strongly dependent on the composition ratio of the stable structures. Thus, after finding the most stable $LiCoO_2$ structure, BO1 searched for the other candidate structures around $LiCoO_2$, which led to a local search. However, because E_{hd} used in BO2 was the relative formation energy measured from the envelope of the convex hull, the composition ratio dependence of E_{hd} was less than that of E_f. Consequently, BO2 performed the structural search over the entire composition ratio space. From the above, BO1 and BO2 were considered to be the exploitation- and exploration-oriented methods, respectively. Therefore, to construct the "true" convex hull efficiently, we need to consider the characterization quantity for the convex hull within the BO framework, in addition to developing the BO algorithm.

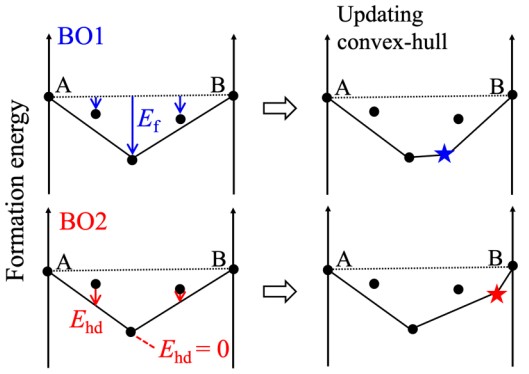

FIG. 5. Schematic image of the convex hull construction for BO1 and BO2 with the A-B binary system. The stars represent the points that succeed in updating the convex hull by each BO method.

B. Relationship between weight density and LCO electrode degradation

Here, we discuss the relationship between the weight densities of the meta-stable CoO_{2-y} structures and the LCO electrode degradation. We found that the finite-temperature effect induces the emergence of the $CoO_{5/3}$ with the O_2 gas release from $Li_{1/3}CoO_2$ under the high-voltage operation shown in Figs. 3(b) and 3(d). Ideally, although the charge/discharge voltage profile directly relates to the convex hull as discussed

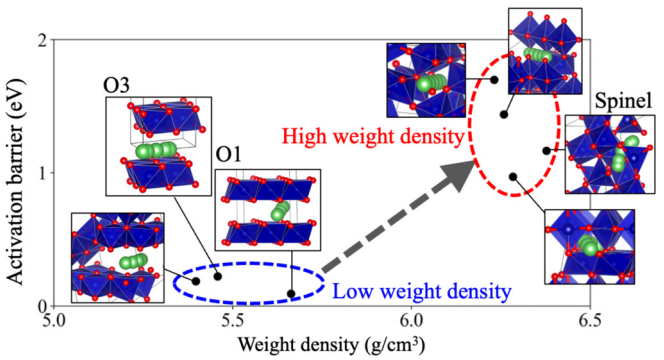

FIG. 6. Activation barriers of Li^+ ion migration in stable and meta-stable CoO_{2-y} and weight densities of CoO_{2-y}.

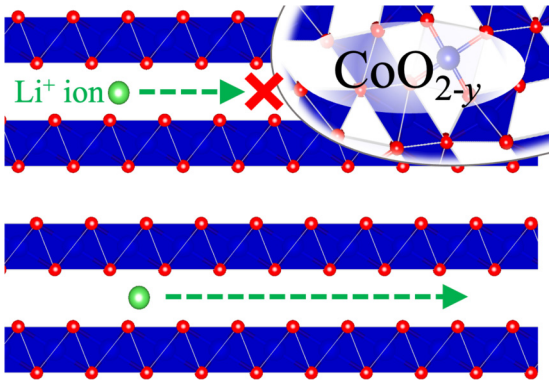

FIG. 7. Schematic image of the Li^+ ion migration in the LCO electrode.

in Sec. II B, forming meta-stable states can be observed over experimental timescales [65–67]. The formation voltages of the meta-stable CoO_{2-y} were 0.4 V higher than that of the stable $CoO_{5/3}$ (see SM [37] for further details). Thus, the meta-stable CoO_{2-y} forms in the high voltage region around the end of the charging cycle with high-capacity utilization.

The weight density of the electrode structure was considered to correlate with the Li^+ ion mobility in the LCO electrode because a high weight density indicated a narrow interstitial region of the crystal. Figure 6 shows the calculated activation barriers of Li^+ ion migration in stable and meta-stable CoO_{2-y} (see SM [37] for computational details). The obtained activation barrier for O3-type (0.2 eV) was consistent with the previous result [68]. CoO_{2-y} with low weight densities have similar activation barriers ($0.1 \sim 0.2$ eV) to O3-type. In contrast, CoO_{2-y} with high weight densities tend to have higher activation barriers ($1.0 \sim 1.7$ eV) than those with low weight densities. Therefore, this calculation result shows the correlation between the mobility of Li^+ ions and weight densities of CoO_{2-y}. In addition, the recent theoretical study found that the large diffusivity of Na^+ ions required the wide faces of Na-S clusters in the sulfide solid electrolytes because the narrow regions yield the high energy barriers for the ion migration [69]. For doped $LiTi_2(PO_4)_3$ (LTP), Lang *et al*. showed an inverse relationship between the Li^+ ion migration barrier and LiO_6 octahedra size in doped LTP [70]. Therefore, from the relation between the activation barrier and weight density, the meta-stable CoO_{2-y} with high weight-densities and non 2D-layered structures might suppress the mobility of Li^+ ions compared with the parent structures (Fig. 7). In addition to the suppressing the Li^+ ion mobility, the once-formed CoO_{2-y} was considered to be partially irreversible because of the high energy barrier required to repair the collapsed layer. Therefore, we considered that the irreversible formation of not only the spinel Co_3O_4 but also CoO_{2-y} with a high weight density suppressed the Li^+ ion migration pathway and deteriorated the electrochemical performance of the LCO electrode.

V. SUMMARY

To reveal the structural changes of $LiCoO_2$ during the battery operation, we employed the CE+BO method to constructing the convex hull of the Li-Co-O phase. In the BO calculation, we adopted hull distance energy as the target variable, which accelerated construction of an accurate convex hull. Therefore, we emphasize that characterization quantity for the convex hull within the BO framework played a significant role in improving the efficiency of CE+BO, in adding to developing the BO algorithm itself. The obtained convex hull provided a charge/discharge voltage curve, that was in reasonable agreement with the experimental results. Finally, we analyzed the meta-stable structures of CoO_{2-y}. Because the formed CoO_{2-y} had a higher weight density than CoO_2, the Li^+ ion conduction path around CoO_{2-y} in the LCO electrode became narrower. Thus, the structural change from CoO_2 to CoO_{2-y} might contribute to cathode degradation during the charge/discharge cycles. These results will provide significant insights into understanding the degradation mechanism of the oxide electrodes. Because the CE+BO method with hull distance is a general formulation, it can easily be applied to other compounds and materials. Hence, we believe that our proposed method will be a powerful tool for revealing structural changes in solid-state materials.

ACKNOWLEDGMENTS

This work was supported by MEXT as the "Program for Promoting Research on the Supercomputer Fugaku" (Fugaku Battery & Fuel Cell Project, Grant No. JPMXP1020200301, and Computational Research on Materials with Better Functions and Durability Toward Sustainable Development, Grant No. JPMXP1020230325). This study was also supported by JSPS KAKENHI (Grant No. JP23K13537). Parallel computations were performed using the Fugaku supercomputer provided by the RIKEN Center for Computational Science (Projects ID: hp200131, ID: hp210173, and ID: hp23020)/FLOW provided by Nagoya University. We also used the computational resources of the supercomputer at the Institute for Solid State Physics at the University of Tokyo. A part of parallel computations was performed using a super-computer provided by Multidisciplinary Cooperative Research Program in CCS, University of Tsukuba.

[1] M. S. Whittingham, Electrical energy storage and intercalation chemistry, Science **192**, 1126 (1976).

[2] D. Larcher and J. -M. Tarascon, Towards greener and more sustainable batteries for electrical energy storage, Nat. Chem. **7**, 19 (2015).

[3] B. Dunn, H. Kamath, and J. M. Tarascon, Electrical energy storage for the grid: A battery of choices, Science **334**, 928 (2011).

[4] K. Mizushima, P. C. Jones, P. J. Wiseman, and J. B. Goodenough, $Li_xCoO_2 (0 < x \leqslant 1)$: A new cathode material

for batteries of high energy density, Solid State Ion. **3-4**, 171 (1981).

[5] S. Li, K. Li, J. Zheng, Q. Zhang, B. Wei, and X. Lu, Structural distortion-induced charge gradient distribution of Co ions in delithiated $LiCoO_2$ dathode, J. Phys. Chem. Lett. **10**, 7537 (2019).

[6] J. Kikkawa, S. Terada, A. Gunji, T. Nagai, K. Kurashima, and K. Kimoto, Chemical states of overcharged $LiCoO_2$ particle surfaces and interiors observed using electron energy-loss spectroscopy, J. Phys. Chem. C **119**, 15823 (2015).

[7] Z. X. Wang, L. J. Liu, L. Q. Chen, and X. J. Huang, Structural and electrochemical characterizations of surface-modified $LiCoO_2$ cathode materials for Li-ion batteries, Solid State Ion. **148**, 335 (2002).

[8] Y. Jiang, C. Qin, P. Yan, and M. Sui, Origins of capacity and voltage fading of $LiCoO_2$ upon high voltage cycling, J. Mater. Chem. A **7**, 20824 (2019).

[9] C. Sun, X. Liao, F. Xia, Y. Zhao, L. Zhang, S. Mu, S. Shi, Y. Li, H. Peng, G. V. Tendeloo, K. Zhao, and J. Wu, High-voltage cycling induced thermal vulnerability in $LiCoO_2$ cathode: Cation loss and oxygen release driven by oxygen vacancy migration, ACS Nano **14**, 6181 (2020).

[10] Y. Lyu, X. Wu, K. Wang, Z. Feng, T. Cheng, Y. Liu, M. Wang, R. Chen, L. Xu, J. Zhou, Y. Lu, and B. Guo, An overview on the advances of $LiCoO_2$ cathodes for lithium-ion batteries, Adv. Energy Mater. **11**, 2000982 (2021).

[11] M. Yoona, Y. Dong, Y. Yoo, S. Myeong, J. Hwang, J. Kim, S. Choi, J. Sung, S. J. Kang, J. Li, and J. Cho, Unveiling nickel chemistry in stabilizing high-voltage cobalt-rich cathodes for lithium-ion batteries, Adv. Funct. Mater. **30**, 1907903 (2020).

[12] P. Hohenberg and W. Kohn, Inhomogeneous electron gas, Phys. Rev. **136**, B864 (1964).

[13] W. Kohn and L. J. Sham, Self-consistent equations including exchange and correlation effects, Phys. Rev. **140**, A1133 (1965).

[14] M. Aykol, S. Kim, and C. Wolverton, Van der Waals interactions in layered lithium cobalt oxides, J. Phys. Chem. C **119**, 19053 (2015).

[15] Y. Ran, Z. Zou, B. Liu, D. Wang, B. Pu, P. Mi, W. Shi, Y. Li, B. He, Z. Lu, X. Lu, B. Li, and S. Shi, Towards prediction of ordered phases in rechargeable battery chemistry via group–subgroup transformation, npj Comput. Mater. **7**, 184 (2021).

[16] H. Euchner and A. Groß, Atomistic modeling of Li- and post-Li-ion batteries, Phys. Rev. Mater. **6**, 040302 (2022).

[17] J. W. D. Connolly and A. R. Williams, Density-functional theory applied to phase transformation in transition-metal alloys, Phys. Rev. B **27**, 5169 (1983).

[18] J. M. Sanchez and F. Ducastelle, Generalized cluster description of multicomponent systems, Physica A **128**, 334 (1984).

[19] A. van de Walle and G. Ceder, Automating first-principles phase diagram calculations, JPE **23**, 348 (2002).

[20] A. van de Walle, Multicomponent multisublattice alloys, nonconfigurational entropy and other additions to the alloy theoretic automated toolkit, Calphad **33**, 266 (2009).

[21] J. H. Chang, D. Kleiven, M. Melander, J. Akola, J. M. G. Lastra, and T. Vegge, CLEASE: A versatile and user-friendly implementation of cluster expansion method, J. Phys.: Condens. Matter **31**, 325901 (2019).

[22] M. Ångqvist, W. A. Muñoz, J. M. Rahm, E. Fransson, C. Durniak, P. Rozyczko, T. H. Rod, and P. Erhart, ICET—A python library for constructing and sampling alloy cluster expansions, Adv. Theo. Sim. **2**, 1900015 (2019).

[23] A. van der Ven, J. C. Thomas, B. Puchala, and A. R. Natarajan, First-principles statistical mechanics of multicomponent crystals, Annu. Rev. Mater. Res. **48**, 27 (2018).

[24] K. Terakura, T. Oguchi, T. Mohri, and K. Watanabe, Electronic theory of the alloy phase stability of Cu-Ag, Cu-Au, and Ag-Au systems, Phys. Rev. B **35**, 2169 (1987).

[25] F. Kuroda, T. Fukushima, and T. Oguchi, First-principles study of magnetism and phase stabilities of V_2 based antiferromagnetic heusler alloys, J. Appl. Phys. **127**, 193904 (2020).

[26] F. Kuroda, T. Fukazawa, and T. Miyake, Ordered and disordered phases in $CaCu_5$-type derived structures: Dumbbell cluster modeling with first-principles calculations, Phys. Rev. Mater. **5**, 124405 (2021).

[27] D. B. Laks, L. G. Ferreira, S. Froyen, and A. Zunger, Efficient cluster expansion for substitutional systems, Phys. Rev. B **46**, 12587 (1992).

[28] A. H. Nguyen, C. W. Rosenbrock, C. S. Reese, and G. L. W. Hart, Robustness of the cluster expansion: Assessing the roles of relaxation and numerical error, Phys. Rev. B **96**, 014107 (2017).

[29] A. Seko and S. Ishiwata, Prediction of perovskite-related structures in $ACuO_{3-x}$(A = Ca, Sr, Ba, Sc, Y, La) using density functional theory and Bayesian optimization., Phys. Rev. B **101**, 134101 (2020).

[30] A. R. Oganov, Y. Ma, A. O. Layakhov, M. Velle, and C. Gatti, Evolutionary crystal structure prediction as a method for the discovery of minerals and materials, Rev. Mineral. Geochem. **71**, 271 (2010).

[31] Y. Wang, J. Lv, L. Zhu, and Y. Ma, CALYPSO: A method for crystal structure prediction, Comput. Phys. Commun. **183**, 2063 (2012).

[32] T. Ishikawa and T. Miyake, Evolutionary construction of a formation-energy convex hull: Practical scheme and application to a carbon-hydrogen binary system, Phys. Rev. B **101**, 214106 (2020).

[33] M. K. Aydinol, A. F. Kohan, G. Ceder, K. Cho, and J. Joannopoulos, *Ab initio* study of lithium intercalation in metal oxides and metal dichalcogenides, Phys. Rev. B **56**, 1354 (1997).

[34] A. van der Ven, M. K. Aydinol, G. Ceder, G. Kresse, and J. Hafner, First-principles investigation of phase stability in Li_xCoO_2, Phys. Rev. B **58**, 2975 (1998).

[35] C. Wolverton and A. Zunger, First-principles prediction of vacancy order-disorder and intercalation battery voltages in Li_xCoO_2, Phys. Rev. Lett. **81**, 606 (1998).

[36] A. R. Natarajan and A. V. der Ven, Machine-learning the configurational energy of multicomponent crystalline solids, npj Comput. Mater. **4**, 56 (2018).

[37] See Supplemental Material at http://link.aps.org/supplemental/10.1103/PhysRevMaterials.7.115402 for computational details and structural information of meta-stable CoO_{2-y}.

[38] S. P. Ong, W. D. Richards, A. Jain, G. Hautier, M. Kocher, S. Cholia, D. Gunter, V. L. Chevrier, K. A. Persson, and G. Ceder, Python materials genomics (pymatgen): A robust, open-source python library for materials analysis, Comput. Mater. Sci. **68**, 314 (2013).

[39] G. Mills, H. Jónsson, and G. K. Schenter, Reversible work transition state theory: Application to dissociative adsorption of hydrogen, Surf. Sci. **324**, 305 (1995).

[40] G. Henkelman, B. P. Uberuaga, and H. Jónsson, A climbing image nudged elastic band method for finding saddle points and minimum energy paths, J. Chem. Phys. **113**, 9901 (2000).

[41] G. Henkelman and H. Jónsson, Improved tangent estimate in the nudged elastic band method for finding minimum energy paths and saddle points, J. Chem. Phys. **113**, 9978 (2000).

[42] M. W. Chase, *Thermochemical Tables* (American Chemical Society, New York, 1998).

[43] P. Wu, G. Hautier, K. Perssonb, and G. Ceder, First principles high throughput screening of oxynitrides for water-splitting photocatalysts, Energy Environ. Sci. **6**, 157 (2013).

[44] P. Giannozzi, S. Baroni, N. Bonini, M. Calandra, R. Car, C. Cavazzoni, D. Ceresoli, G. L. Chiarotti, M. Cococcioni, and I. Dabo, QUANTUM ESPRESSO: A modular and open-source software project for quantum simulations of materials, J. Phys.: Condens. Matter **21**, 395502 (2009).

[45] P. Giannozzi Jr, O. Andreussi, T. Brumme, O. Bunau, M. B. Nardelli, M. Calandra, R. Car, C. Cavazzoni, D. Ceresoli, and M. Cococcioni, Advanced capabilities for materials modelling with QUANTUM ESPRESSO, J. Phys.: Condens. Matter **29**, 465901 (2017).

[46] D. Vanderbilt, Soft self-consistent pseudopotentials in a generalized eigenvalue formalism, Phys. Rev. B **41**, 7892(R) (1990).

[47] A. Dal Corso, Pseudopotentials periodic table: From H to Pu, Comput. Mater. Sci. **95**, 337 (2014).

[48] J. P. Perdew, K. Burke, and M. Ernzerhof, Generalized gradient approximation made simple, Phys. Rev. Lett. **77**, 3865 (1996).

[49] V. I. Anisimov, I. V. Solovyev, M. A. Korotin, M. T. Czyk, and G. A. Sawatzky, Density-functional theory and NiO photoemission spectra, Phys. Rev. B **48**, 16929 (1993).

[50] J. Klimeš, D. R. Bowler, and A. Michaelides, Van der Waals density functionals applied to solids, Phys. Rev. B **83**, 195131 (2011).

[51] L. Wang, T. Maxisch, and G. Ceder, Oxidation energies of transition metal oxides within the GGA+U framework, Phys. Rev. B **73**, 195107 (2006).

[52] R. Tamura, K. Yoshimi, K. Terayama, T. Ueno, and K. Tsuda, Bayesian optimization package: Physbo, Comput. Phys. Commun. **278**, 108405 (2022).

[53] T. Ueno, T. D. Rhone, Z. Hou, T. Mizoguchi, and K. Tsuda, Combo: An efficient Bayesian optimization library for materials science, Mater. Discovery **4**, 18 (2016).

[54] S. Ju, T. Shiga, L. Feng, Z. Hou, K. Tsuda, and J. Shiomi, Designing nanostructures for phonon transport via Bayesian optimization, Phys. Rev. X **7**, 021024 (2017).

[55] T. Yamashita, N. Sato, H. Kino, T. Miyake, K. Tsuda, and T. Oguchi, Crystal structure prediction accelerated by Bayesian optimization, Phys. Rev. Mater. **2**, 013803 (2018).

[56] T. Fukazawa, Y. Harashima, Z. Hou, and T. Miyake, Bayesian optimization of chemical composition: A comprehensive framework and its application to $R\mathrm{Fe}_{12}$-type magnet compounds, Phys. Rev. Mater. **3**, 053807 (2019).

[57] G. L. W. Hart and R. W. Forcade, Algorithm for generating derivative structures, Phys. Rev. B **77**, 224115 (2008).

[58] G. L. W. Hart and R. W. Forcade, Generating derivative structures from multilattices: Algorithm and application to hcp alloys, Phys. Rev. B **80**, 014120 (2009).

[59] G. G. Amatucci, J. M. Tarascon, and L. C. Klein, CoO_2, the end member of the Li_xCoO_2 solid solution, J. Electrochem. Soc. **143**, 1114 (1996).

[60] Z. Chen, Z. Lu, and J. R. Dahn, Staging phase transitions in Li_xCoO_2, J. Electrochem. Soc. **149**, A1604 (2002).

[61] K. Momma and F. Izumi, VESTA 3 for three-dimensional visualization of crystal, volumetric, and morphology data, J. Appl. Crystallogr. **44**, 1272 (2011).

[62] Z. Chen and J. R. Dahn, Methods to obtain excellent capacity retention in $LiCoO_2$ cycled to 4.5 V, Electrochim. Acta **49**, 1079 (2004).

[63] J. Haruyama, S. Takagi, K. Shimoda, I. Watanabe, K. Sodeyama, T. Ikeshoji, and M. Otani, Thermodynamic analysis of Li-intercalated graphite by first-principles calculations with vibrational and configurational contributions, J. Phys. Chem. C **125**, 27891 (2021).

[64] W. Sun, S. T. Dacek, S. P. Ong, G. Hautier, A. Jain, W. D. Richards, A. C. Gamst, K. A. Persson, and G. Ceder, The thermodynamic scale of inorganic crystalline metastability, Sci. Adv. **2**, e1600225 (2016).

[65] Y. Orikasa, T. Maeda, Y. Koyama, H. Murayama, K. Fukuda, H. Tanida, H. Arai, E. Matsubara, Y. Uchimoto, and Z. Ogumi, Direct observation of a metastable crystal phase of Li_xFePO_4 under electrochemical phase transition, J. Am. Chem. Soc. **135**, 5497 (2013).

[66] H. Liu, F. C. Strobridge, O. J. Borkiewicz, K. M. Wiaderek, K. W. Chapman, P. J. Chupas, and C. P. Grey, Capturing metastable structures during high-rate cycling of $LiFePO_4$ nanoparticle electrodes, Science **344**, 1252817 (2014).

[67] M. P. Mercer, C. Peng, C. Soares, H. E. Hoster, and D. Kramer, Voltage hysteresis during lithiation/delithiation of graphite associated with meta-stable carbon stackings, J. Mater. Chem. A **9**, 492 (2021).

[68] M. Okubo, T. Yoshinori, H. Zhou, T. Kudo, and I. Honma, Determination of activation energy for Li Ion diffusion in electrodes, J. Phys. Chem. B **113**, 2840 (2009).

[69] S.-H. Jang, Y. Tateyama, and R. Jalem, High-throughput data-driven prediction of stable high-performance Na-ion sulfide solid electrolytes, Adv. Funct. Mater. **32**, 2206036 (2022).

[70] B. Lang, B. Ziebarth, and C. Elsässer, Lithium ion conduction in $LiTi_2(PO_4)_3$ and related compounds based on the nasicon structure: A first-principles study, Chem. Mater. **27**, 5040 (2015).